

## Magnetized filamentary gas flows feeding the young embedded cluster in Serpens South

THUSHARA G.S. PILLAI,<sup>1,2</sup> DAN P. CLEMENS,<sup>3</sup> STEFAN REISSL,<sup>4</sup> PHILIP C. MYERS,<sup>5</sup>  
JENS KAUFFMANN,<sup>6</sup> ENRIQUE LOPEZ-RODRIGUEZ,<sup>7</sup> F. O. ALVES,<sup>8</sup>  
G. A. P. FRANCO,<sup>9</sup> JONATHAN HENSHAW,<sup>10</sup> KARL M. MENTEN,<sup>11</sup>  
FUMITAKA NAKAMURA,<sup>12</sup> DANIEL SEIFRIED,<sup>13</sup> KOJI SUGITANI,<sup>14</sup> AND  
HELMUT WIESEMAYER<sup>11</sup>

<sup>1</sup>*Institute for Astrophysical Research, Boston University, 725 Commonwealth Avenue, Boston MA, 02215, USA*

<sup>2</sup>*Max-Planck-Institut für Radioastronomie, Auf dem Hügel 69, D-53121 Bonn, Germany*

<sup>3</sup>*Institute for Astrophysical Research, Boston University, 725 Commonwealth Avenue, Boston, MA 02215, USA*

<sup>4</sup>*Universität Heidelberg, Zentrum für Astronomie, Institut für Theoretische Astrophysik, Albert-Ueberle-Str. 2, 69120 Heidelberg, Germany*

<sup>5</sup>*Harvard-Smithsonian Center for Astrophysics, 60 Garden Street, Cambridge, MA 02138 USA*

<sup>6</sup>*Haystack Observatory, Massachusetts Institute of Technology, Westford, MA 01886, USA*

<sup>7</sup>*SOFIA Science Center, NASA Ames Research Center, Moffett Field, CA 94035, USA*

<sup>8</sup>*Max-Planck-Institut für extraterrestrische Physik, Giessenbachstr. 1, 85748 Garching, Germany*

<sup>9</sup>*Departamento de Física ICEX/UFMG, Caixa Postal 702, 30.123-970 Belo Horizonte, Brazil*

<sup>10</sup>*Max-Planck-Institute for Astronomy, Königstuhl 17, 69117 Heidelberg, Germany*

<sup>11</sup>*Max-Planck-Institut für Radioastronomie, Auf dem Hügel 69, D-53121 Bonn, Germany*

<sup>12</sup>*National Astronomical Observatory of Japan, 2-21-1 Osawa, Mitaka, Tokyo 181-8588, Japan*

<sup>13</sup>*Universität zu Köln, I. Physikalisches Institut, Zùlpicher Str. 77, 50937 Köln, Germany*

<sup>14</sup>*Graduate School of Natural Sciences, Nagoya City University, Mizuho-ku, Nagoya, Aichi 467-8501, Japan*

### ABSTRACT

Observations indicate that molecular clouds are strongly magnetized, and that magnetic fields influence the formation of stars. A key observation supporting the conclusion that molecular clouds are significantly magnetized is that the orientation of their internal structure is closely related to that of the magnetic field. At low column densities the structure aligns parallel with the field, whereas at higher column densities, the gas structure is typically oriented perpendicular to magnetic fields, with a transition at visual extinctions  $A_V \gtrsim 3$  mag. Here we use far-infrared polarimetric observations from the HAWC+ polarimeter on SOFIA to report the discovery of a further transition in relative orientation, i.e., a return to parallel alignment at  $A_V \gtrsim 21$  mag in parts of the Serpens South cloud. This transition appears to be caused by gas flow and indicates that magnetic supercriticality sets in near  $A_V \gtrsim 21$  mag, allowing grav-

itational collapse and star cluster formation to occur even in the presence of relatively strong magnetic fields.

## INTRODUCTION

A fundamental question in star formation physics is “What processes create and support dense interstellar medium (ISM) filaments and regulate the star formation within them?” While magnetic fields are predicted to play an important role in the formation of dense filamentary structures, of dense cores, and ultimately of stars within them, the importance of magnetic fields relative to turbulence and gravity remains poorly constrained<sup>1,2</sup>.

Dust emission polarization observations at 353 GHz by the *Planck* satellite have shown ordered magnetic field structures towards the Gould Belt clouds in the solar neighborhood<sup>3</sup>. Studies have further quantified the importance of magnetic fields via an assessment of the relative orientation between column density ( $N_{\text{H}}$ ) structures (filaments) and the plane of the sky magnetic field ( $B_{\text{pos}}$ ). Within a star forming complex, low column density features are preferentially aligned parallel to the magnetic field, while at high column density, they tend to be perpendicular to the field. A transition between the modes is observed for an  $A_V$  range of  $\simeq 2.7 - 3.5$  mag<sup>3,4</sup>. Optical and near-infrared (NIR) dust extinction polarization observations of lower column density regions of filaments show similar behaviour<sup>5,6,7,8,9</sup>.

Yet, *Planck*'s  $\sim 10'$  beam, which corresponds to linear scales of  $\sim 1$  pc  $\cdot (d/345$  pc), was unable to resolve details of the magnetic field structure on dense cores size scales ( $< 0.1$  pc). The specific role of magnetic fields in shaping how the filaments fragment into cores and on to form stars and clusters thus remains unknown.

The Serpens South cloud resides in the Aquila Rift complex<sup>10</sup> at a distance of 436 pc<sup>11</sup>. Figure 1 shows that this cloud harbors a prominent hub-filament system (HFS), i.e. a system of filaments that radiate from a denser hub (a zone with protostellar formation<sup>12</sup>). Based on its high ratio of protostellar (Class 0/I) sources relative to pre-main sequence (Class II/III) sources, the star cluster in the Serpens South hub is likely the youngest cluster in the local neighborhood<sup>10</sup>. The extreme youth and proximity of this HFS makes it an ideal laboratory for testing the role of magnetic fields in a filamentary dark cloud in an early stage of star cluster formation.

## THE DATA

Serpens South was observed using the HAWC+ polarimeter on the 2.7-m SOFIA telescope, using the far-infrared (FIR) *E*-band ( $\lambda_C = 214 \mu\text{m}$ ,  $\Delta\lambda = 44 \mu\text{m}$ ; see Methods). The main data products were the fractional polarization ( $P$ ), position angle (PA), and their uncertainties ( $\sigma_P$ ,  $\sigma_{PA}$ ).

For regions of the cloud with weak detections, it was necessary to smooth the data to achieve adequate signal-to-noise ratios in polarization ( $\text{PSNR} \equiv P'/\sigma_P$ ), where,  $P'$  is the debiased fractional polarization and  $\sigma_P$ , its uncertainty (see Methods). Radiative aligned torques<sup>13</sup> cause dust grains in dense clouds to align such that their major axes, which are sensed by FIR **emission** polarimetry, are oriented perpendicular to the magnetic field<sup>14</sup>. Therefore, the HAWC+ vectors discussed throughout the text have been rotated by  $90^\circ$  relative to the electric field orientation to denote the plane of the sky magnetic field  $B_{\text{pos}}$ . The resultant polarization vectors are shown in Figure 1.

The NIR **extinction** polarization vectors presented in Figure 1 were adopted from literature<sup>5</sup>, selecting their *H*-band data. Only polarization values that satisfied the additional quality criteria discussed in Kusune et al<sup>15</sup> were considered. The NIR vectors directly sense  $B_{\text{pos}}$  and so have not been rotated.

Additionally, we used a *Herschel* gas ( $\text{H}_2$ ) column density map derived by the *Herschel* Gould Belt Survey (HGBS<sup>16</sup>). The map was based on *Herschel* 70 to 500  $\mu\text{m}$  images<sup>17</sup> at a resolution of  $36''$ . We used the standard conversion factor<sup>18</sup> between column density and visual extinction,  $N_{\text{H}_2} = 9.4 \times 10^{20} \text{ cm}^{-2} (A_V \text{ mag})^{-1}$ .

## RESULTS

Figure 1 shows the Serpens South cloud, with NIR and HAWC+ magnetic field orientations overlaid as pseudo (headless) vectors. We partitioned the sky presentation of the cloud system into a hub (MAINHUB) that harbors the Serpens South Star Cluster and into three filaments (FIL1, FIL2, FIL3) that appear to connect to the hub (see Figure 1). We delineated the extents of these filament regions using ellipses. The ellipses were chosen to maximize the number of significant polarization detections for each region but to have minimal overlap between adjacent ellipse regions (Methods). The FIL3 region was removed from the remaining analysis steps as it contained too few HAWC+ polarimetric detections.

The large-scale magnetic field orientation follows a generally NE-SW direction that is mostly perpendicular to the gas distribution within the MAINHUB region. The magnetic field orientations with respect to the gas distributions within FIL1 and FIL2 are more complex. The large-scale magnetic field traced by NIR polarimetry is mostly perpendicular to the gas filaments. But, the magnetic field orientations seen on the smaller scales traced by the new FIR polarimetry do not appear to follow the same patterns seen on the larger, NIR-traced, scales.

We quantified the relation between cloud gas structures and magnetic fields by measuring the relative projected orientations between the filaments and the magnetic

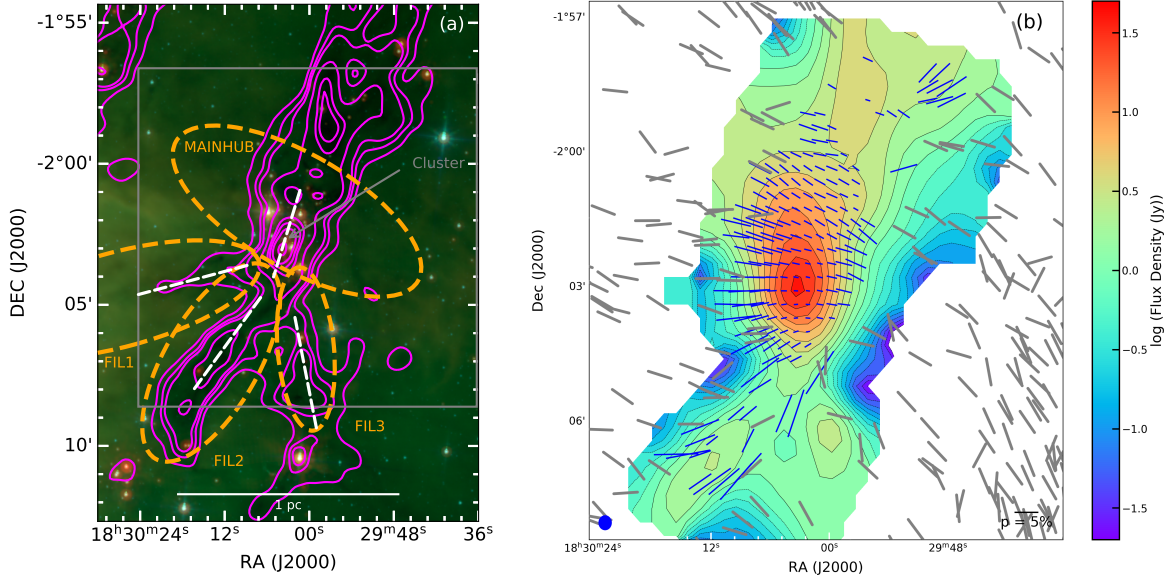


**Figure 1.** The Serpens South cloud as seen by Spitzer (a), HAWC+ intensity imaging (color scale in panel b), and polarimetry from NIR and HAWC+ data (vectors in b). The three-color overview map is generated from data acquired with the MIPS  $24\ \mu\text{m}$  (red), IRAC  $8\ \mu\text{m}$  (blue) and IRAC  $5.8\ \mu\text{m}$  (green) sensors. The grey box in (a) shows the region mapped with HAWC+, magenta contours correspond to the  $\text{H}_2$  column densities from *Herschel* data<sup>16</sup> at  $A_V$  values of 15, 20, 30, 45, 70, 85, 110, and 150 mag, and the dashed white lines show the median RHT-traced filament orientations (see text). Orange ellipses delimit the regions containing MAINHUB, FIL1 and FIL2. White solid line of 1 pc shows a physical length scale of 3.26 light years. Panel (b) presents HAWC+  $214\ \mu\text{m}$  intensity (color), and polarimetry from NIR<sup>5</sup> (grey) and HAWC+  $214\ \mu\text{m}$  data (blue, this work) at  $\text{PSNR} > 3$  and  $\text{PSNR} > 2$ , respectively, tracing the magnetic field orientations, corresponding to  $\sigma_{PA} < 10(14)^\circ$ . The blue circle at lower left shows the HAWC+  $214\ \mu\text{m}$  beamsize. The reference percentage polarization length for HAWC+ is shown in the lower center, while the lengths of the NIR vectors were set to be identical.

fields traced via polarimetry. We characterized the filament orientations using the Rolling Hough Transform (RHT<sup>19</sup>), an image processing tool that determines orientations of linear structures (Methods). We constructed histograms of RHT angles and magnetic field orientations within the MAINHUB, FIL1, and FIL2 regions. We also calculated median RHT angles and magnetic field orientations within each elliptical region. The results are shown in Fig. 2. At the large spatial scales of the elliptical regions ( $0.1 - 0.5\ \text{pc}$ ), the NIR polarization orientations for FIL1 show a narrow distribution whose median value is  $32 \pm 2^\circ$  offset from being parallel to the RHT-traced gas filament orientation. For FIL2, the median NIR field orientation is  $73 \pm 5^\circ$  offset from the filament. For MAINHUB, the NIR field orientation is  $95 \pm 12^\circ$  from the filament angle.

These offset angle values reveal the NIR-traced magnetic field is perpendicular to the gas structures within the FIL2 and MAINHUB zones. At smaller spatial scales ( $< 0.1\ \text{pc}$ ), however, the smoothed HAWC+ observations of the FIL2 region show magnetic field orientations closer to being parallel to the gas filament elongation

(medians offset by  $22 \pm 3^\circ$ ). For MAINHUB, the large-scale perpendicular relative orientation is preserved down to the smaller, FIR-traced scales (medians offset by  $87 \pm 1^\circ$ ). Different ellipse sizes were tried and found to yield consistent results.

FIL2, the FIR-brightest southern filament connecting to the central hub (see Fig. 1), thus shows a distinct change in magnetic field orientation, from being perpendicular to the moderate column density gas structure to being parallel to the high column density one. For every FIL2 NIR and FIR dust polarization detection that met our SNR criteria, we extracted the corresponding magnetic field orientation ( $B_{\text{pos}}$ ) and the *Herschel*-based  $\text{H}_2$  column density and converted the latter to visual extinction  $A_V$ . Fixing the filament orientation  $X_{\text{FIL}}$  to the  $144^\circ$  median value from Figure 2, we computed its difference to each magnetic field orientation ( $X_{\text{B}_{\text{pos}}} - X_{\text{FIL}}$ ). The results are summarized in Figure 3. The Figure reveals the strong, systematic change in relative orientation between the magnetic field and the filament direction that occurs near an extinction threshold  $A_V \sim 21$  mag.

## DISCUSSION

*Evidence for magnetized filamentary accretion in FIL2*—At 10 arcmin resolution, Planck Collaboration Int. XXXV<sup>3</sup> found, for Gould Belt molecular clouds, a change in relative orientations between magnetic fields and filament elongations, from being generally parallel to being perpendicular, occurs at  $A_V > 2.7$  mag. A similar analysis of the Aquila rift<sup>4</sup>, which encompasses Serpens South, found an orientation transition at  $A_V \sim 3.5$  mag. These studies revealed the dynamically important role played by magnetic fields in collecting and channeling matter into present molecular cloud configurations.

The observations presented here of just such a star-forming filament show that this picture is more complex. While the perpendicular magnetic field orientation is preserved for sightlines piercing the dense hub, the moderate column density FIL2 region filament exhibits a magnetic field orientation that undergoes a change back to being parallel to the filament. The change in relative orientations between the magnetic field and the filament elongation occurs at about  $A_V \sim 21$  mag, as shown in Fig. 3.

This transition threshold was determined as follows. Adopted 30% uncertainties for the pixels in the *Herschel*-based column density map, following Section 4.6 of Konyves et al.<sup>17</sup>, we binned the map pixels that matched to NIR or FIR polarization detections into logarithmically spaced bins of  $A_V$ . From the resulting distributions, we determined the first, second (median), and third quartiles for every bin. The span of the data that fell within the interquartile range, i.e. within the first and the third quartile, is shown as the orange shaded region in Fig. 3. The transition threshold was taken to be where the median values of relative orientations cross  $45^\circ$ , namely 21 mag. The  $A_V$  range of the transition is shown by the gray zone in the Figure. It is bounded by where the first quartiles of the low  $A_V$  data points cross  $45^\circ$ , at 17 mag,

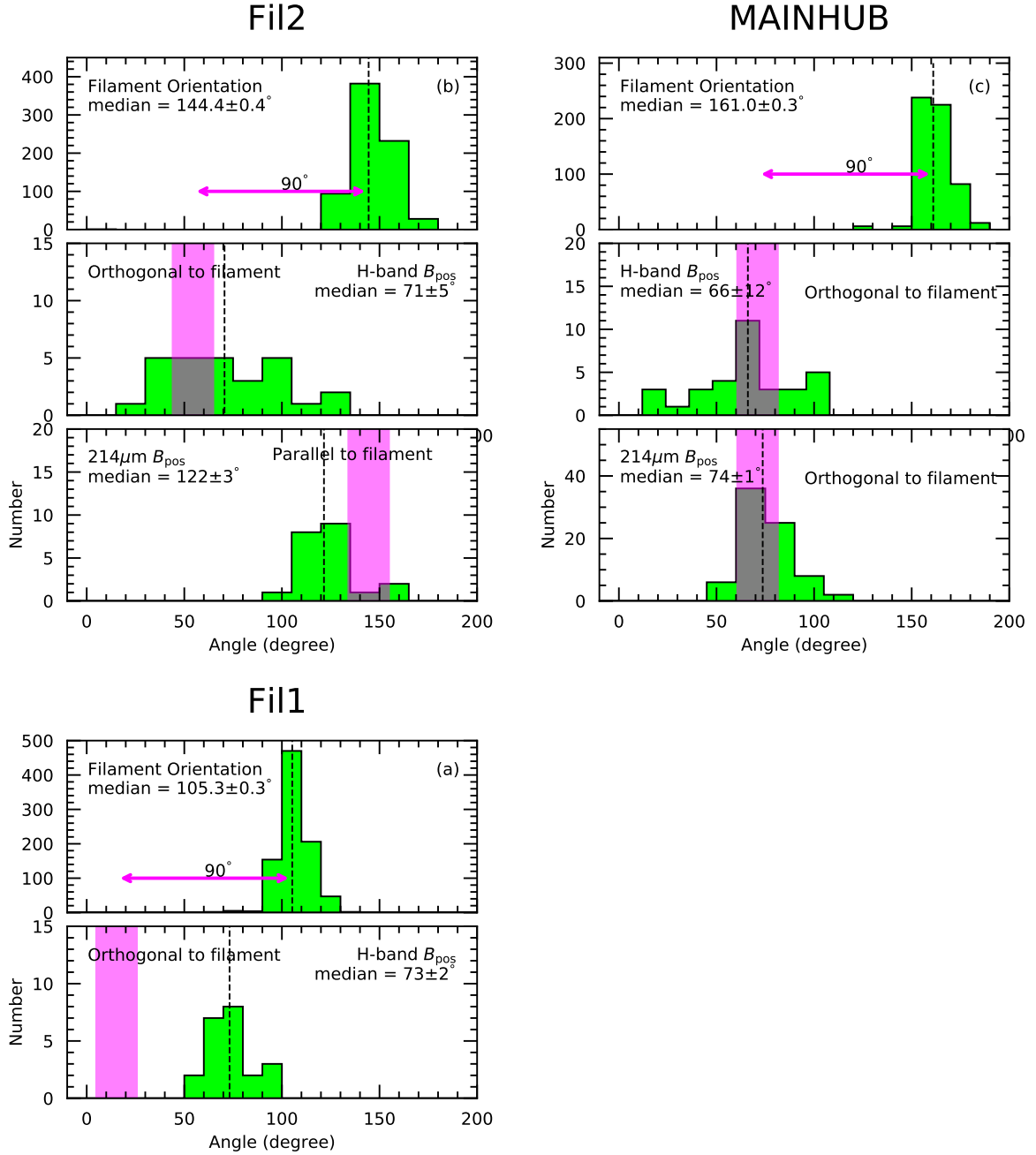


**Figure 2.** Distributions of filament angles derived from RHT analysis (top panels), magnetic field orientations in the NIR (second panels), and in the FIR (third panels, if present) for the FIL1 (a), FIL2 (b), and MAINHUB (c) elliptical regions. No HAWC+ detections have been found towards FIL1. The black dashed lines represent the medians of each distribution and the uncertainties shown are the errors of the means. The purple shaded bars represent the ranges that would conform to having either a parallel and perpendicular orientation of the field ( $\pm 10^\circ$ ) with respect to the filament angle.

and the where the third quartiles of the high  $A_V$  data points similarly cross that line, at 29 mag.

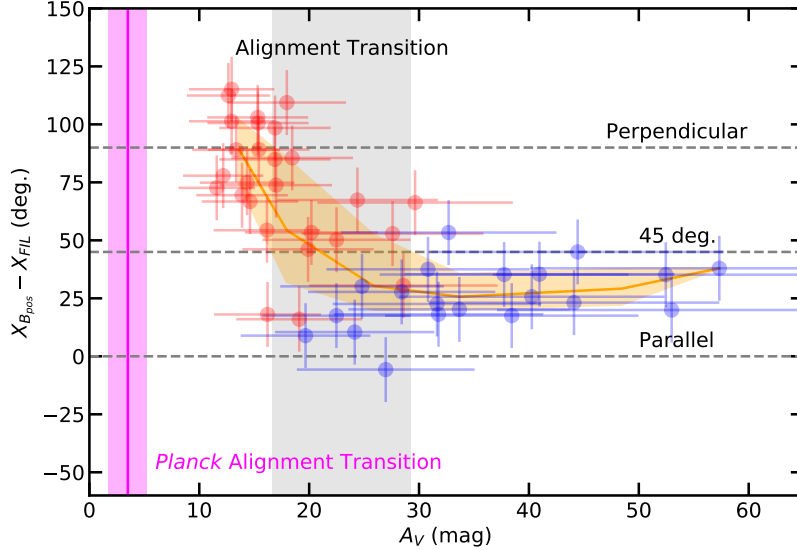


**Figure 3.** Distribution of relative orientations of the FIL2 gas filament with respect to  $B_{\text{pos}}$  as a function of  $A_V$ . The NIR  $B_{\text{pos}}$  are shown as red filled circles and the FIR as blue filled circles. Their corresponding  $1\sigma$  uncertainties are shown as errorbars. The three dashed lines show parallel,  $45^\circ$ , and perpendicular orientations of the magnetic field with the filament. The orange area captures the interquartile ranges for all data versus  $A_V$ . The vertical gray rectangle highlights where the median relative orientation crosses  $45^\circ$ , with width related to the uncertainty of the crossing value. This indicates where the transition from a perpendicular to parallel field orientation occurs. The magenta bar represents the lower  $A_V$ , first alignment transition suggested by *Planck* data, for the parallel to perpendicular transition near  $A_V \sim 3.5$  mag<sup>4</sup>.

We interpret this changing magnetic field orientation in the FIL2 region as evidence for gravity dragging the denser gas, and entraining the frozen-in large-scale magnetic field, to become a parallel flow of matter toward the MAINHUB region. In this interpretation, the FIL1, FIL2, and FIL3 region filaments act as accretion channels to funnel gas to the dense hub.

Numerical simulations predict that magnetic field orientations should follow such gravity-induced flows inside dense filaments<sup>20,21,22</sup>. Magnetized accretion flows had been expected and have been observed on protostellar envelope and smaller disk size scales ( $\leq 500$  AU)<sup>23,24,25,26</sup>. Evidence for such accretion flows have been found in the smooth velocity gradients in  $\text{N}_2\text{H}^+ 1\rightarrow 0$  in the FIL2 region filament<sup>27</sup>(see also Fernandez-Lopez et al.<sup>28</sup>). Field-parallel orientations have been observed recently in a dense filament in Orion’s OMC1 region<sup>29</sup> as well as in a distant, hub-filament infrared dark cloud<sup>30</sup>. The combined NIR and FIR polarimetric observations reported here show that filamentary accretion flows affect the local magnetic field orientation and thereby shape the magnetic field structure on filament size scales. A consistent picture emerges of a system of filaments merging into a hub via gas flows along, or entraining, magnetic field lines.

*Field Strengths*—Magnetic field support of filaments of the FIL2 region type must lose to gravitational collapse close to where the new change in orientation has been discovered, in order to explain the onset of star formation. The mass-to-magnetic-flux ratio,  $M/\Phi_B$ , reaches its critical value,  $(M/\Phi_B)_{\text{cr}}$ , and induces a filament to collapse and form stars, if  $(M/\Phi_B) > (M/\Phi_B)_{\text{cr}}$  (the magnetically supercritical condition). Following McKee and Ostriker<sup>31</sup>, and recast into typical physical units<sup>32</sup>,

$$\frac{(M/\Phi_B)}{(M/\Phi_B)_{\text{cr}}} \approx 0.76 \left( \frac{\langle N_{\text{H}_2} \rangle}{10^{23} \text{ cm}^{-2}} \right) \left( \frac{B_{\text{tot}}}{1 \text{ mG}} \right)^{-1}. \quad (1)$$

For a transition at  $A_V \sim 21$  mag,  $(M/\Phi_B)/(M/\Phi_B)_{\text{cr}} \geq 1$  is fulfilled if  $B_{\text{tot}} \leq 140 \mu\text{G}$ .

We adopted a spheroidal density distribution and assumed flux-freezing<sup>33,34</sup> to obtain an estimate of the magnetic field strength for the MAINHUB region. These assumptions fully constrain the relative geometry of the density distribution and the magnetic field, but not their absolute scaling. We assumed that the dense core is magnetically supercritical within the  $A_V \sim 40$  mag contour (column density  $\sim 4 \times 10^{22} \text{ cm}^{-2}$ ), where the central core becomes prominent relative to the surrounding material. This additional constrain fixes the distribution of density and magnetic field in absolute terms, resulting in a central magnetic field strength of  $\sim 870 \mu\text{G}$  and a central density of  $\rho_0 = 6.3 \times 10^5 \text{ cm}^{-3}$  for the MAINHUB core in Serpens South.

This field strength estimate may be compared to values obtained from the empirical relation<sup>1</sup>,  $B = B_0 \cdot (n_{\text{H}_2}/10^4 \text{ cm}^{-3})^{0.65}$  with  $B_0 \lesssim 150 \mu\text{G}$ . For the FIL2 region filament, we obtained a density estimate of  $6.4 \times 10^4 \text{ cm}^{-3}$ , appropriate for the transition at  $A_V \sim 21$  mag, through dividing the *Herschel* column density values there by an approximate filament width<sup>35</sup> of  $\sim 0.1$  pc. Under these assumptions, the Crutcher relation suggests  $B \lesssim 500 \mu\text{G}$ , consistent with the  $140 \mu\text{G}$  value obtained assuming magnetic supercriticality for the filament. For the MAINHUB region, the Crutcher relation suggests  $B \lesssim 2 \text{ mG}$  at the modeled central density of  $6.3 \times 10^5 \text{ cm}^{-3}$ , while we estimated  $870 \mu\text{G}$  from flux-freezing.

That our estimates of  $B$  are consistent with those suggested by the Crutcher relation is remarkable, because our investigation probed (in particular in FIL2) gas that is less disturbed by star formation than the regions from which the Crutcher relation was derived (i.e., traced by masers and CN emission connected to very active star formation), and thus potentially more representative of the initial conditions for star formation.

*Effects of protostellar radiation on fractional polarization*—While the mean magnetic field is well ordered along the NE-SW direction, the FIR polarized fraction is not uniform in the MAINHUB region, where the greatest number of HAWC+ polarization detections are present. A significant decrease in the polarization degree is evident in Fig. 1 towards the brightest emission peak in MAINHUB.

In Figure 4, we show the debiased polarization fraction as a function of the FIR  $214 \mu\text{m}$  total intensity (Stokes  $I$ ) and the weighted least squares power-law fit to the



data. We do not apply any signal-to-noise cutoffs for the fractional polarization. This is because polarization fraction is a positive quantity, and follows a Rice distribution and therefore would introduce a bias to high polarization values in regions with low PSNR<sup>36</sup>. We derive a best-fit power-law slope of  $b = -0.55 \pm 0.03$ .

A relatively wide range in this slope has been recently reported, with  $b = -0.34$  towards the externally-illuminated Oph A region<sup>37</sup>, while starless cores such as Pipe 109/FeSt I-457 show<sup>38,39</sup>  $b \approx -1$ . In well-illuminated regions of molecular clouds, dust grains align with their minor axes parallel to the local magnetic field direction. However, because radiation does not sufficiently penetrate the denser parts of clouds, the efficiency of the alignment with the local magnetic field may fall significantly (see review by Andersson et al.<sup>14</sup>). The observed slope of  $b \sim -0.5$  in Serpens South is thus intermediate between the two extreme cases: strong radiation inducing perfect dust grain alignment and weak radiation causing no alignment. The intermediate value for our slope suggests that while the efficiency of grain alignment decreases linearly with increasing optical depth, FIR polarimetry still probes the magnetic field in the densest parts of this cloud. This is a rather surprising result given the high extinction towards the center of the Serpens South cluster, of the order  $A_V \sim 150$  mag.

In order to probe the nature of the alignment in more detail, we modeled the FIR dust polarization observations, based on the known properties of the cloud’s density profile, its temperature, and its star-formation state, as described in Methods. The modeling used the radiative transfer (RT) code POLARIS<sup>40</sup> to create simulated maps of dust temperature, RATs, and dust polarization for two setups. Setup “A” used an external diffuse interstellar radiation field (ISRF) as the only radiation source for dust heating and grain alignment. Setup “B” included the ISRF as well as internal sources of radiation from the protostars in the Serpens South Star Cluster (see Methods).

The resulting correlations between polarization fraction  $P_{\text{frac}}$  and Stokes  $I$  are shown in Fig. 4. Setup A shows a steeper slope because the external ISRF is extinguished with increasing optical depth into the filament, causing the dust alignment efficiency to decrease with  $A_V$  or Stokes  $I$ . In setup B, the radiation from the embedded YSOs increases the dust alignment in the cloud core center, leading to a shallower slope in the Figure. The slope for our observations agrees better with the setup B model than with the setup A one. At the greater  $A_V$  (Stokes  $I$ ) end of the Figure’s right panel, the setup B distribution shows a rise in fractional polarization, consistent with the localized influence of internal illumination on grain alignment at the center of the cluster. However, this trend is not resolved in our FIR data. In summary, embedded YSOs can cause a relatively shallow slope for the correlation, consistent with our FIR observations.

## CONCLUSIONS

Large-scale *Planck* observations of Gould Belt clouds find a transition in relative orientation between magnetic fields and gas filaments from being parallel for

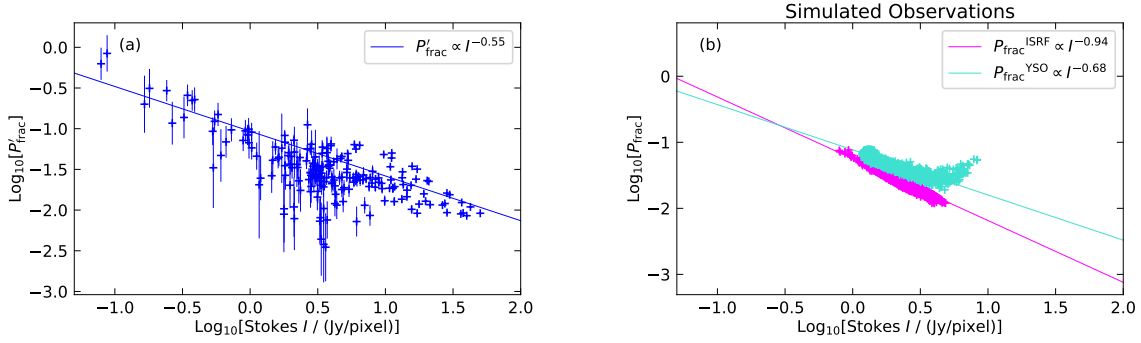


**Figure 4.** Comparison of the correlation between fractional polarization and column density towards MAINHUB in Serpens South using HAWC+ 214  $\mu\text{m}$  (panel [a]) and in simulated data (panel [b]).  $P'_{\text{frac}}$  is the debiased fractional polarization from observations and  $P_{\text{frac}}$  is the fractional polarization. Observational uncertainties are defined in the Methods section. The solid line in panel (a) shows a least square fit. Simulated observations from POLARIS in panel (b) were conducted with ISRF alone (setup A, magenta crosses) and including the effect of a cluster of YSOs (setup B, turquoise crosses). The corresponding best fits to the model predictions are also shown.

$A_V \leq 2.7 - 3.5$  mag to being perpendicular beyond that  $A_V$  range. Recent submm observations show magnetic field orientations parallel to dense filaments in a few star-forming regions<sup>29,30</sup>, but does not capture a transition.

The Serpens South cloud is a dense, cluster-forming, hub-filament system in the Aquila complex where we have used the HAWC+ FIR polarimeter instrument on SOFIA, in conjunction with published NIR polarimetry, to discover a new transition occurring at even greater  $A_V$  values. This new transition reveals the change of the magnetic field from being perpendicular to a large-scale, modest  $A_V$ , filament gas structure to becoming a smaller-scale magnetic field that is parallel to the densest gas structure beyond  $A_V \sim 20$  mag. In addition, the slope of the observed decrease in fractional polarization with  $A_V$  is better modeled when the external ISRF is augmented by inclusion of illumination from the embedded protostars in the Serpens South cluster, enhancing the link of magnetic fields traced by FIR polarimetry with the dense, opaque gas.

This favors a scenario of gas filaments merging into a central hub, reorienting or entraining the magnetic field in the dense gas flows. Recent kinematic observations show evidence for gas flows along such filaments towards the hub in systems, including in Serpens South<sup>41,42,27</sup>. Thus, at  $< 0.1$  pc scale, we find observational evidence for the feeding of gas, containing significant magnetic fields, into a low-mass, cluster-forming region.

## ACKNOWLEDGMENTS

Based in part on observations made with the NASA/DLR Stratospheric Observatory for Infrared Astronomy (SOFIA). SOFIA is jointly operated by the Universities Space Research Association, Inc. (USRA), under NASA contract NAS2-97001, and the Deutsches SOFIA Institut (DSI) under DLR contract 50 OK 0901 to the University of Stuttgart. We sincerely thank the reviewers for their valuable comments that improved the clarity of this manuscript. Financial support for this work was provided to TP by DLR through award # 50 OR 1719. Darren Dowell, the SOFIA HAWC+ team, the SOFIA flight and ground crews, and the USRA SOFIA Project teams developed the SOFIA observatory, the HAWC+ instrument, performed the airborne observations, processed and calibrated the data, and delivered science-ready data products. DPC acknowledges support funder NSF AST 18-14531, USRA SOF 4-0026, and NASA NNX15AE51G. DS acknowledges the support of the Bonn-Cologne Graduate School, which is funded through the German Excellence Initiative and funding by the Deutsche Forschungsgemeinschaft (DFG) via the Collaborative Research Center SFB 956 Conditions and Impact of Star Formation (subprojects C5 and C6). GAPF is partially supported by CNPq and FAPEMIG.

This research has made use of data from the Herschel Gould Belt survey (HGBS) project (<http://gouldbelt-herschel.cea.fr>, André et al. 2010).

## AUTHOR CONTRIBUTIONS

T.P. led the SOFIA proposal, data analysis, interpretation of the data, and the paper writing. Other authors contributed to the writing of the manuscript. D.P.C., S.R., P.C.M., and J.K. participated in the data analysis. E.L-R. led the SOFIA data reduction. F.O.A. and G.A.F. conducted near-IR polarization observations. K.S. provided the published near-IR polarization data used in this study. J.H., K.M.M, F.N, D.S., and H.W. provided expertise in molecular cloud studies.

## METHODS

*Observations*—Serpens South was observed (PI: Pillai, ID: 05\_0206) on 2017 May 12-13 using HAWC+<sup>43,44,45</sup> with the 2.7-m SOFIA telescope. HAWC+ polarimetric observations simultaneously imaged two orthogonal components of linear polarization onto two detector arrays of up to  $32 \times 40$  pixels each. Observations performed using the *E*-band provided a pixel scale of  $9.37''$ , a beam size of  $18.2''$  and an instantaneous field-of-view of up to  $4.2 \times 6.2$  arcmin<sup>2</sup>.

Observations were conducted using the standard chop-nod polarimetric mode. Specifically, a four-position dither pattern with an offset of three pixels ( $28''$ ) was used. At each dither position, a halfwave plate stepped through four distinct position angles, and images were obtained at each step. Observations used nod times of 40 s, with a chop-frequency of 10.2 Hz. Final polarimetric images were composed from observations of two different sky pointing directions. Based on the morphology of

the source from *Herschel* observations, chopping did not switch into significant flux contribution from diffuse extended emission or compact sources.

The data were reduced using HAWC\_DRP pipeline v1.3.0 and custom python routines. Detail data reduction steps can be found in Harper et al.<sup>45</sup>. In summary, the raw data were demodulated, chop-nod and background subtracted, flux calibrated, and Stokes parameters were estimated along with their uncertainties. Fractional polarization ( $P$ ), position angle (PA), and their uncertainties were evaluated using Eqs. 1, 2, 4, and 5 of Gordon et al.<sup>46</sup>. The final  $P$  and PA were corrected using measured instrumental polarizations and were then debiased. The debiased fractional polarization was derived from the fractional polarization as<sup>47</sup>  $P' = \sqrt{(P^2 - \sigma_P^2)}$ .

For regions of the cloud with weak detections (e.g., FIL2), it was necessary to smooth the polarization data to increase PSNR. The smoothing followed the approach detailed in Clemens et al.<sup>48</sup>. From a variety of trial smoothing beams, we chose a gaussian kernel FWHM = 18.2" ( $\sim 4$  HAWC+ pixels) to smooth the SOFIA-delivered Stokes  $QI$ ,  $UI$ , and  $I$  maps. This yielded a maximum number of independent synthetic pixels with PSNR > 2.0 ( $\sigma_{PA} < 14^\circ$ ).

The near-IR  $H$ -band data were adopted from Sugitani et al.<sup>5</sup>. Only values that satisfied the following criteria were extracted:  $P/\sigma_P > 3.0$  and  $P^*/3 < P < 3P^*$ , where  $P^* = 2.73([H - K_s] - 0.2)$  is the best-fit color dependence for  $H$ -band stars with  $\sigma_P < 0.3\%$ , following Kusune et al.<sup>15</sup>.

*Measuring Filament Orientations*—We quantified the relationships between cloud structures and magnetic fields by measuring their relative projected orientations. To characterize filament orientations, we used the RHT<sup>19</sup>.

The regions containing the Serpens South filaments were delimited by ellipses. These ellipses were chosen to maximize the numbers of significant polarization detections contained within each while minimizing overlap between adjacent ellipses. Since the MAINHUB gas appears in relative isolation, there is little confusion with neighboring (FIL) ellipses. For it, we established a large encompassing ellipse that extends well beyond the high-column-density material in MAINHUB. This ensures that many NIR detections are contained in that zone. Narrower ellipses were chosen for FIL1 and FIL2 to avoid overlaps. Note that ellipse long-axis orientations are not meant to represent filament or hub gas structure elongations. The ellipses merely define regions of interest associated with the dominant gas structures contained within their boundaries.

To find linear structures in images and to determine their orientations, RHT uses three input parameters. Following the convention in Clark et al.<sup>19</sup>, these are a smoothing kernel diameter ( $D_K$ ), a diameter of the window used to roll across the image ( $D_W$ ), and an intensity threshold ( $Z$ ) above which data are extracted. Our input image was the *Herschel* dust column density map. Our choices of RHT parameters were  $D_K = 55$  pixels (= 5.7 arcmin),  $D_W = 15$  pixels (= 1.5 arcmin), and  $Z = 70\%$  of the

map peak intensity. We explored input variable values and found a wide combination of values still extracted the same filaments, ensuring robust results.

*Flux-freezing model*—The Serpens South cloud harbors a centrally condensed core whose surrounding polarization directions suggest the ordered pattern expected for flux freezing<sup>34</sup> combined with a random component which may be attributed to turbulent motions. To estimate the maximum magnetic field strength associated with the star-forming Serpens South core, we assumed that the core is magnetically supercritical within the  $A_V \sim 40$  mag contour (column density  $\sim 4 \times 10^{22} \text{cm}^{-2}$ ), which is where the core appears to emerge from its harboring filament. The field strength was obtained from the flux-freezing model<sup>33,34</sup>, and from a model of the core as prolate spheroid<sup>49</sup>.

The core density model was obtained by fitting  $p = 2$  Plummer<sup>50</sup> column density profiles (consistent with the cloud structure<sup>17</sup>) to the principal axes of the *Herschel*-based core column density map shown in Figure 1. This modeling gave a central volume density  $\rho_0 = 6.3 \times 10^5 \text{cm}^{-3}$  and scale length  $R_{\text{flat}} = 0.03 \text{pc}$ . These parameters were used to obtain expressions for the core volume density and mean volume density, per Myers et al.<sup>34</sup>.

Then, as shown in Myers et al.<sup>34</sup>, the peak field strength in the core equatorial plane can be expressed as

$$B_0 = [(8\pi/3) G^{1/2} \rho_0 r_0] [3 (\xi_c - \arctan \xi_c)]^{1/3}, \quad (2)$$

where  $\xi_c = x_c/r_0$  is the dimensionless radius of the  $A_V \sim 40$  mag ( $N_{\text{H}_2} = 4 \times 10^{22} \text{cm}^{-2}$ ) map contour. For Serpens South, we found  $\xi_c = 2$ . Evaluating equation (2) yielded  $B_0 = 0.87 \text{mG}$ , which serves better than an order-of-magnitude estimate, based on the assumption of the core being magnetically supercritical within the  $A_V \sim 40$  mag contour. This estimate is useful, but we caution that it harbors ill-constrained, difficult to quantify uncertainties.

*Radiative Transfer using POLARIS*—We used the RT code POLARIS<sup>40</sup> to create simulated dust temperature, RATs, and dust polarization maps on a cylindrical grid. The cylindrical grid had a length of 1 pc and a maximum radius of 0.5 pc. We applied a Plummer density profile  $\rho(r) = \rho_0 [1 + (r/R_{\text{flat}})^2]^{-p/2}$  with parameters  $R_{\text{flat}} = 0.03 \text{pc}$  and  $p = 2$ , from the previous section.

The density  $\rho_0$  was chosen, upon line of sight integration, to match the observed central column density of  $N_{\text{H}_2} = 1.6 \times 10^{23} \text{cm}^{-2}$ . This resulted in a total gas mass of  $M_{\text{gas}} = 518 M_{\odot}$  within the grid. The magnetic field was assumed to penetrate perpendicular to the spine of the cylinder, with a constant strength of  $B = 100 \mu\text{G}$ . The gas temperature was a free parameter, set initially at  $T_{\text{gas}} = 15 \text{K}$  to encompass the upper limit of the measured gas temperature from  $\text{NH}_3$  observations<sup>51</sup>.

For the dust properties, we used pre-calculated values of oblate grains with typical composition of 62.5% graphite, 37.5% silicate<sup>52</sup>, an aspect ratio of 1:2 and a mass

ratio of  $M_{\text{dust}}/M_{\text{gas}} = 0.01$ . The grain size  $a$  distribution followed  $n(a) \propto a^{-3.5}$  with cut-offs at  $a_{\text{min}} = 5$  nm and  $a_{\text{max}} = 500$  nm, typical for dense clouds<sup>53</sup>.

We conducted two different RT simulation setups to calculate grain alignment efficiencies, following RAT theory<sup>40</sup>.

For setup A, an external, diffuse ISRF<sup>54</sup> was the only radiation source. For setup B, the luminosities and effective temperatures of the 37 Serpens South Class I YSOs reported<sup>55</sup>, were included, in addition to the ISRF. The simulated stars were placed randomly along the axial extent of the model cylinder, while their radial offsets from the spine were drawn randomly from a Gaussian distribution with a FWHM of 0.015 pc. The latter was adopted to be bounded by the stellar surface density distribution measured by Gutermuth et al.<sup>10</sup>. Setup A resulted in a range of final dust temperatures, up to  $T_{\text{dust}} = 20$  K at the edge of the filament model and about  $T_{\text{dust}} = 8$  K toward the spine. Regarding the RATs, dust grains larger than  $a = 181$  nm were well-aligned to the local magnetic field when close to the filament's surface, whereas even the largest grains were not well-aligned at the location of the cylinder spine. The setup B YSOs brought RATs alignment to  $a = 125$  nm in the close proximity of the YSOs. Finally, we simulated synthetic polarization maps as being projected onto a detector with  $64 \times 64$  pixels in a distance of 436 pc convolved with a beam of 19 arcsec.

## REFERENCES

- [1]Crutcher, R. M. Magnetic Fields in Molecular Clouds. *ARA&A* **50**, 29–63 (2012).
- [2]Li, H.-B. *et al.* The Link Between Magnetic Fields and Cloud/Star Formation. *Protostars and Planets VI* 101–123 (2014).
- [3]Planck Collaboration XXXV *et al.* Planck intermediate results. XXXV. Probing the role of the magnetic field in the formation of structure in molecular clouds. *A&A* **586**, A138 (2016).
- [4]Soler, J. D. *et al.* The relation between the column density structures and the magnetic field orientation in the Vela C molecular complex. *A&A* **603**, A64 (2017).
- [5]Sugitani, K. *et al.* Near-infrared-imaging Polarimetry Toward Serpens South: Revealing the Importance of the Magnetic Field. *ApJ* **734**, 63 (2011).
- [6]Palmeirim, P. *et al.* Herschel view of the Taurus B211/3 filament and striations: evidence of filamentary growth? *A&A* **550**, A38 (2013).
- [7]Franco, G. A. P. & Alves, F. O. Tracing the Magnetic Field Morphology of the Lupus I Molecular Cloud. *ApJ* **807**, 5 (2015).
- [8]Santos, F. P., Busquet, G., Franco, G. A. P., Girart, J. M. & Zhang, Q. Magnetically Dominated Parallel Interstellar Filaments in the Infrared Dark Cloud G14.225-0.506. *ApJ* **832**, 186 (2016).
- [9]Soler, J. D. Using Herschel and Planck observations to delineate the role of magnetic fields in molecular cloud structure. *A&A* **629**, A96 (2019).
- [10]Gutermuth, R. A. *et al.* The Spitzer Gould Belt Survey of Large Nearby Interstellar Clouds: Discovery of a Dense Embedded Cluster in the Serpens-Aquila Rift. *ApJL* **673**, L151–L154 (2008).

- [11]Ortiz-León, G. N. *et al.* Gaia-DR2 Confirms VLBA Parallaxes in Ophiuchus, Serpens, and Aquila. *ApJL* **869**, L33 (2018).
- [12]Myers, P. C. Filamentary Structure of Star-forming Complexes. *ApJ* **700**, 1609–1625 (2009).
- [13]Lazarian, A. & Hoang, T. Radiative torques: analytical model and basic properties. *MNRAS* **378**, 910–946 (2007).
- [14]Andersson, B.-G., Lazarian, A. & Vaillancourt, J. E. Interstellar Dust Grain Alignment. *ARA&A* **53**, 501–539 (2015).
- [15]Kusune, T. *et al.* Magnetic field structure in Serpens South. *PASJ* (2019).
- [16]André, P. *et al.* From filamentary clouds to prestellar cores to the stellar IMF: Initial highlights from the Herschel Gould Belt Survey. *A&A* **518**, L102+ (2010).
- [17]Könyves, V. *et al.* A census of dense cores in the Aquila cloud complex: SPIRE/PACS observations from the Herschel Gould Belt survey. *A&A* **584**, A91 (2015).
- [18]Kauffmann, J., Bertoldi, F., Bourke, T. L., Evans, N. J., II & Lee, C. W. MAMBO mapping of Spitzer c2d small clouds and cores. *A&A* **487**, 993–1017 (2008).
- [19]Clark, S. E., Peek, J. E. G. & Putman, M. E. Magnetically Aligned H I Fibers and the Rolling Hough Transform. *ApJ* **789**, 82 (2014).
- [20]Körtgen, B. & Banerjee, R. Impact of magnetic fields on molecular cloud formation and evolution. *MNRAS* **451**, 3340–3353 (2015).
- [21]Gómez, G. C., Vázquez-Semadeni, E. & Zamora-Avilés, M. The magnetic field structure in molecular cloud filaments. *MNRAS* **480**, 2939–2944 (2018).
- [22]Li, P. S., Klein, R. I. & McKee, C. F. Formation of stellar clusters in magnetized, filamentary infrared dark clouds. *MNRAS* **473**, 4220–4241 (2018).
- [23]Sadavoy, S. I. *et al.* Dust Polarization toward Embedded Protostars in Ophiuchus with ALMA. II. IRAS 16293-2422. *ApJ* **869**, 115 (2018).
- [24]Maury, A. J. *et al.* Magnetically regulated collapse in the B335 protostar? I. ALMA observations of the polarized dust emission. *MNRAS* **477**, 2760–2765 (2018).
- [25]Takahashi, S. *et al.* ALMA High Angular Resolution Polarization Study: An Extremely Young Class 0 Source, OMC-3/MMS 6. *ApJ* **872**, 70 (2019).
- [26]Le Gouellec, V. J. M. *et al.* Characterizing Magnetic Field Morphologies in Three Serpens Protostellar Cores with ALMA. *ApJ* **885**, 106 (2019).
- [27]Kirk, H. *et al.* Filamentary Accretion Flows in the Embedded Serpens South Protocluster. *ApJ* **766**, 115 (2013).
- [28]Fernández-López, M. *et al.* CARMA Large Area Star Formation Survey: Observational Analysis of Filaments in the Serpens South Molecular Cloud. *ApJL* **790**, L19 (2014).
- [29]Monsch, K. *et al.* Dense Gas Kinematics and a Narrow Filament in the Orion A OMC1 Region Using NH<sub>3</sub>. *ApJ* **861**, 77 (2018).
- [30]Liu, T. *et al.* A Holistic Perspective on the Dynamics of G035.39-00.33: The Interplay between Gas and Magnetic Fields. *ApJ* **859**, 151 (2018).
- [31]McKee, C. F. & Ostriker, E. C. Theory of Star Formation. *ARA&A* **45**, 565–687 (2007).
- [32]Pillai, T. *et al.* Magnetic Fields in High-mass Infrared Dark Clouds. *ApJ* **799**, 74 (2015).
- [33]Mestel, L. The magnetic field of a contracting gas cloud. I, Strict flux-freezing. *MNRAS* **133**, 265 (1966).
- [34]Myers, P. C., Basu, S. & Auddy, S. Magnetic Field Structure in Spheroidal Star-forming Clouds. *ApJ* **868**, 51 (2018).
- [35]Hill, T. *et al.* Resolving the Vela C ridge with P-ArTéMiS and Herschel. *A&A* **548**, L6 (2012).

- [36] Montier, L. *et al.* Polarization measurement analysis. II. Best estimators of polarization fraction and angle. *A&A* **574**, A136 (2015).
- [37] Pattle, K. *et al.* JCMT BISTRO Survey Observations of the Ophiuchus Molecular Cloud: Dust Grain Alignment Properties Inferred Using a Ricean Noise Model. *ApJ* **880**, 27 (2019).
- [38] Alves, F. O. *et al.* On the radiation driven alignment of dust grains: Detection of the polarization hole in a starless core (Corrigendum). *A&A* **574**, C4 (2015).
- [39] Kandori, R. *et al.* Distortion of Magnetic Fields in a Starless Core. V. Near-infrared and Submillimeter Polarization in FeSt 1-457. *ApJ* **868**, 94 (2018).
- [40] Reissl, S., Wolf, S. & Brauer, R. Radiative transfer with POLARIS. I. Analysis of magnetic fields through synthetic dust continuum polarization measurements. *A&A* **593**, A87 (2016).
- [41] Schneider, N. *et al.* Dynamic star formation in the massive DR21 filament. *A&A* **520**, A49+ (2010).
- [42] Peretto, N. *et al.* Global collapse of molecular clouds as a formation mechanism for the most massive stars. *A&A* **555**, A112 (2013).
- [43] Vaillancourt, J. E. *et al.* Far-infrared polarimetry from the Stratospheric Observatory for Infrared Astronomy **6678**, 66780D (2007).
- [44] Dowell, C. D. *et al.* *HAWCPol: a first-generation far-infrared polarimeter for SOFIA*, vol. 7735 of *Society of Photo-Optical Instrumentation Engineers (SPIE) Conference Series*, 77356H (2010).
- [45] Harper, D. A. *et al.* HAWC+, the Far-Infrared Camera and Polarimeter for SOFIA. *Journal of Astronomical Instrumentation* **7**, 1840008–1025 (2018).
- [46] Gordon, M. S. *et al.* SOFIA Community Science I: HAWC+ Polarimetry of 30 Doradus. *arXiv e-prints* arXiv:1811.03100 (2018).
- [47] Serkowski, K. *Polarization techniques*. (1974).
- [48] Clemens, D. P. *et al.* Magnetic Field Uniformity Across the GF 9-2 YSO, L1082C Dense Core, and GF 9 Filamentary Dark Cloud. *ApJ* **867**, 79 (2018).
- [49] Myers, P. C. Star-forming Filament Models. *ApJ* **838**, 10 (2017).
- [50] Plummer, H. C. On the problem of distribution in globular star clusters. *MNRAS* **71**, 460–470 (1911).
- [51] Friesen, R. K., Bourke, T. L., Di Francesco, J., Gutermuth, R. & Myers, P. C. The Fragmentation and Stability of Hierarchical Structure in Serpens South. *ApJ* **833**, 204 (2016).
- [52] Reissl, S., Seifried, D., Wolf, S., Banerjee, R. & Klessen, R. S. The origin of dust polarization in molecular outflows. *A&A* **603**, A71 (2017).
- [53] Martin, P. G. & Whittet, D. C. B. Interstellar Extinction and Polarization in the Infrared. *ApJ* **357**, 113 (1990).
- [54] Mathis, J. S., Mezger, P. G. & Panagia, N. Interstellar radiation field and dust temperatures in the diffuse interstellar matter and in giant molecular clouds. *A&A* **500**, 259–276 (1983).
- [55] Dunham, M. M. *et al.* Young Stellar Objects in the Gould Belt. *ApJS* **220**, 11 (2015).